Am J Transl Res 2024;16(10):5525-5538
www.ajtr.org /ISSN:1943-8141/AJTR0157262

Original Article

3D visualization of cellular and molecular distributions in human crystalline lenses at different ages

Wei Hu[1,2*], Xiaoyu Tong[1,2*], Lu Zhang[3,4*], Jiajia Li[1,2], Kaijing Zhou[3,4], Wenhan Lu[5], Jiemei Shi[5], Wenjing Wang[3,4], Mengdi Zhang[3,4], Yicong Wang[1,2], Wendong Han[6], Liyipeng Chen[7], Jin Li[3,4], Yi Feng[1,2]

[1]Department of Integrative Medicine and Neurobiology, School of Basic Medical Sciences, Institutes of Brain Science, Brain Science Collaborative Innovation Center, State Key Laboratory of Medical Neurobiology, Institute of Acupuncture and Moxibustion, Fudan Institutes of Integrative Medicine, Fudan University, Shanghai 200032, China; [2]Shanghai Key Laboratory of Acupuncture Mechanism and Acupoint Function, Shanghai 200032, China; [3]National Clinical Research Center for Ocular Diseases, Eye Hospital, Wenzhou Medical University, Wenzhou 325027, Zhejiang, China; [4]State Key Laboratory of Ophthalmology, Optometry and Visual Science, Eye Hospital, Wenzhou Medical University, Wenzhou 325027, Zhejiang, China; [5]Department of Ophthalmology and Vision Science, Eye and ENT Hospital, Fudan University, Shanghai 200031, China; [6]Biosafety Level 3 Laboratory and Shanghai Medical College Fudan University, Shanghai 200032, China; [7]Binjiang College of Zhejiang Chinese Medical University, Hangzhou 310053, Zhejiang, China. [*]Equal contributors.

Received April 18, 2024; Accepted August 24, 2024; Epub October 15, 2024; Published October 30, 2024

Abstract: Background: The human lens is a highly organized tissue, and it is constructed of delicate inner architectures that ensure its transparency. However, the pattern of cell distribution in the intact lens has rarely been observed or traced in a three-dimensional (3D) perspective. Methods: Here, we modified and compared three different kinds of tissue transparency methods to investigate the cellular and molecular changes in the human lens at different ages from a 3D perspective. Results: First, we analyzed the general 3D parameters of cleared human lenses from 6 months to 72 years of age and found that the equator proportion remained constant with age (23.05% ± 0.36). Next, we visualized the cellular distribution patterns in the anterior capsule and equator, as well as the distribution of cortical fiber cells. Interestingly, we observed the accumulation of equatorial epithelium in adolescents and the asymmetrical denucleation of cortical fiber cells in the elderly. Zonula occludens-1 and tropomyosin receptor kinase A were also identified in the pre-equatorial germinative zone, and its presence decreased when comparing lenses of a 17-year-old to those of a 49-year-old. Conclusion: We present a 3D cellular and molecular reconstruction of the human lens, illustrating the observed alterations in human lens epithelial cells across different ages.

Keywords: Lens, optical transparency technology, 3D visualization, cataract

Introduction

The lens is one of the most crucial optical components of human eyes, and it consists of the capsule, epithelial layers, and cortical fibers [1]. The transparency, morphology, and hardness of the lens change along with aging, and under pathologic conditions such changes can lead to diseases like presbyopia and cataract [2-5]. Thus, a particular focus on lens-related research has been how the lens changes over time [6].

Much effort has been made to further understand the morphology and architecture of the lens because these form the basis for maintaining the transparency of the lens [7, 8]. The lens is composed primarily of the outer capsule and inner fibers and undergoes dynamic changes over the lifetime. Epithelial cells are closely packed into the capsule, and these cells denucleate to form fibers. It is widely recognized that the pre-equatorial zone is where new cells germinate [9, 10]. However, direct imaging proof and the detailed cellular distribution patterns have remained elusive as have been the cellular and molecular changes that occur during aging. Various gross geometric features of the lens can be quantified and applied in clinical diagnoses, such as optical coherence tomogra-

phy (OCT), which measures the volume, equatorial diameter, and plane position of the lens [11]. Three-dimensional (3D) *in vivo* modeling of the lens can be achieved with magnetic resonance imaging [12], and the delicate microscopic and higher dimensional features of the lens are current topics of lens research. Traditional methods, including flat-mounting and confocal microscopy techniques, have been applied to observe the epithelial cells, fiber cells, and capsule as well as to provide more quantitative details like epithelial cell density and fiber shapes and diameters [13, 14]. However, these micro-level observation techniques are incompatible with large-scale 3D views, thus impeding the creation of 3D panoramic views of the cellular arrangement of the lens.

Recently, tissue clearing techniques have been developed to obtain 3D views of the molecular and cellular components of large-scale tissue specimens [15]. The main advantage of these techniques is that they combine clearing, labeling, and imaging and thus allow the specific molecular visualization of the whole organ and the quantitative analysis of its 3D parameters [16]. Previously developed techniques rely on fixation using paraformaldehyde or formalin, but this can cause opacity of the lens, resulting in light scattering [17]. Tissue clearing is the initial process in obtaining 3D images of the entire lens, and the entire mouse eye globe has been effectively rendered transparent in previous studies [18-20]. However, when isolated lenses are removed from their neighboring eye tissues differences in the expansion capacity between fibers and the capsule make it challenging to clear such lenses [21]. In addition, none of the tissue clearing methods have been applied in human eyes, thus emphasizing the possible research value of the current work.

In the present study, we compared the modified tissue clearing methods for human lenses and obtained a 3D map of the lens's cellular characteristics. We observed changes in the expression of zonula occludens-1 (ZO-1) and tropomyosin receptor kinase A (TrkA) across different ages, thus demonstrating that optical transparency technology is useful in constructing a comprehensive molecular and cellular map of the human lens.

Materials and methods

The reagents (including antibodies), equipment, and software are shown in Supplementary Table 1.

Human lens samples

The present study followed the guidelines of the Declaration of Helsinki and was approved by the Ethics Committee of Wenzhou Medical University, Zhejiang, China (2020-132-K-117-02). Lenses from healthy humans without eye diseases prior to death and donated for corneal transplantation were obtained from the Eye Bank of Wenzhou Medical University. Four lenses were obtained from a 72-year-old (72 Y) and 49-year-old (49 Y), while one lens was obtained from a 17-year-old (17 Y) and one from a 6-month-old (6 M). All isolated intact lenses were obtained within 1 to 2 days after the donors died and were put into 4% paraformaldehyde (PFA) solution overnight at 4°C to start the clearing process (Supplementary Table 2).

e-CLARITY (enucleation-Clear Lipid-exchanged Acrylamide-hybridized Rigid Imaging/immunostaining/in situ-hybridization-compatible Tissue hYdrogel) for lens clearing

Enucleation, nucleus delivery, and hydrogel embedding were performed prior to e-CLARITY. These methods were adapted from those widely used in clinical cataract surgery, but in our case, the core of the lens was removed and only the capsule was kept [22, 23]. The posterior capsule of the isolated lens was removed as a 6 mm diameter circle. Then, the posterior cortex and nuclei could be easily sucked out of the lens through the hole left by the posterior capsule (Supplementary Figure 1A). The hollowed-out lens was refilled with 4°C hydrogel solution and incubated in a water bath at 37°C for about 5-6 hours until the hydrogel solidified.

The e-CLARITY process was performed according to previous work [24-26]. The entire procedure was performed on a shaker in a 37°C incubator. Briefly, after removing the extra gel around the lens the lens was soaked in the clearing solution (8% SDS solution/200 mM sodium borate buffer) for about one week until the lens turned clear. The clearing solution was

changed to fresh solution every day in order to prevent bursting of the capsule and to accelerate the clearing process. For immunostaining, the lens was first incubated with primary antibodies against ZO-1 (1:50 dilution, mouse monoclonal, catalog #33-9100, Invitrogen) and then incubated with secondary antibodies (1:100 dilution, Alexa Fluor 488 anti-mouse, AB_2633275, Thermo Fisher Scientific) and 4',6-diamidino-2-phenylindole (DAPI, 1:100 dilution, D9542, Sigma-Aldrich), all of which were diluted in 1× PBS/0.01% bovine serum albumin. These two antibody incubations lasted for 48 h, and the tubes were covered with aluminum foil. The lenses were washed three times with 1× PBS/0.01% bovine serum albumin for 24 h before adding the primary antibody, between the primary and secondary antibodies, and after adding the secondary antibody. Before imaging, the lenses were incubated in Easy Index as the refractive index matching solution for about 48 h.

CUBIC (Clear, Unobstructed Brain/body Imaging Cocktails and computational analysis) for lens clearing

The CUBIC lens clearing was performed according to the protocol of Susaki et al. and our previous work [27-29]. The entire CUBIC process was conducted on a shaker in a 37°C incubator. Briefly, the lens was first embedded in CUBIC clearing solution (50% for 3 hours and 100% for 3 days, consisting of 25% urea, 25% tetraethylenediamine, and 15% Triton X-100) supplemented with propidium iodide (PI, 1:100 dilution, P1304MP, Thermo Fisher Scientific). The lens was then treated with Scale solution (25% urea, 50% sucrose, and 10% triethanolamine) for refractive index homogenization (50% solution until the lens sank to the bottom and then 100% solution until the tissue cleared, usually about 48 h) and then immersed in a mixture of 50% mineral oil and 50% silicone oil for imaging.

iDISCO (Immunolabeling-enabled three-Dimensional Imaging of Solvent-Cleared organs) for lens clearing

The iDISCO process was performed according to the protocol of Renier et al. [30]. The lens was first dehydrated in a series of methanol in PBS (20%, 40%, 60%, 80%, 100%, for 1 h each at room temperature) and incubated in 66% dichloromethane/33% methanol with shaking at 4°C overnight. The lens was then bleached with 5% H_2O_2/95% methanol at 4°C overnight followed by rehydration in a series of methanol in PBS (80%, 60%, 40%, 20%, for 1 h each at room temperature). Before immunostaining, permeabilization and blocking were performed to improve the efficiency of staining. The immunostaining process was the same as for e-CLARITY discussed above, except for the primary antibody being TrkA (1:50 dilution, mouse monoclonal, MA5-15509, Invitrogen) and the washing solution being changed to PTwH solution. The process of methanol dehydration and dichloromethane incubation was also the same as above. Finally, the lens was incubated with dibenzyl ether until cleared, usually taking about 48 h.

Versatile tiling light sheet imaging and image analysis

A versatile tiling light sheet microscope [31] (Nuohai Life Science Co., Ltd.) was used to image the intact transparent lens, and Imaris software (Imaris 9.7, Oxford Instruments PLC, UK) was used to perform the 3D image analysis on our workstation (Intel Xeon W-2245 CPU @ 3.9 GHz, RAM 128 GB, x64 Win10). The original microscope image files contained four light sheet phase positions per layer scan, and these were first combined to make one image for each scan. Imaris File Converter and Imaris Stitcher (Imaris 9.7, Oxford Instruments PLC, UK) were then used to transfer the 2D images series to the 3D file. For quantification, basic Imaris Surpass tree items were used, including *surface* and *spots*. All of the data were autocalibrated based on the coefficient of expansion when comparing post-clearing to the original. The *surface* item was used to reconstruct the anterior capsule, the equator, and the whole lens surface, while the *spots* item was used to reconstruct the nuclei. Both the *surface* and *spots* were built automatically based on the immunofluorescent intensity, with the estimated diameter set to 6 μm to facilitate detection of the nuclei with the *spots* item.

Basic direct 3D parameters were semiautomatically calculated after imaging according to the restricted definition [32]. In brief, the lens and equatorial thicknesses are the perpendicular distances from the anterior to the posterior of

the lens and the equator, and these were calculated as the number of layers multiplied by the distance between the layers. The equator proportion was estimated as the thickness of the equator divided by the thickness of the whole lens. The lens equatorial diameter was the diameter of the equator in the coronal section, and the equatorial plane position was the distance from the anterior pole to the equatorial plane. In addition, the lens surface area and volume were calculated for the whole lens.

Three indirect 3D parameters were automatically calculated after reconstruction in this study, including the number of *spots*, the area and sphericity of the *surface*, and the centroid distance between *spots* and *surface* (Supplementary Figure 1B). The sphericity was defined as the ratio between the surface area (A_1) of a sphere with the same volume as the reconstructed object and the surface area (A_2) of the reconstructed sphere [33], the centroid was defined as the geometric center of an assumed homogeneous mass, and the thickness was calculated semi-automatically as the distance between the sharpest signal edges under the same fluorescence threshold.

Statistical analysis

We evenly divided each sample into four regions for statistical analysis. All 3D parameters were analyzed by GraphPad Prism (v 8.0.2, GraphPad Software, Inc., San Diego, CA, USA) and are presented as means ± standard errors. Using the Shapiro-Wilk test, the distributions were shown to be normally distributed. One-way ANOVA and Dunnett's comparison were performed to calculate the significance between the groups. Fit spline analysis was applied to fit the trend changes. $P < 0.05$ was set as the limit for statistical significance.

Results

Human lenses cleared by e-CLARITY, CUBIC, and iDISCO

For the clearing of human lenses, we used modified versions of three different methods of lens clearing based on reported experiences in clearing the entire mouse eye globe, including e-CLARITY, CUBIC, and iDISCO [18-20]. All three methods resulted in the clearing and immunostaining of lenses in less than 17 days (**Figure 1**, Supplementary Figure 2A), among which e-CLARITY took the longest time (17 days) and CUBIC took the shortest (about 11 days). We modified the e-CLARITY process by adding the enucleation step prior to hydrogel embedding and by increasing the concentration of SDS to 8% (**Figure 1**). For the CUBIC method, we added PI in the CUBIC clearing solution to shorten the time needed for immunostaining. Lastly, in the modification of iDISCO we changed the immunostaining time to 48 h for antibody embedding.

To compare the clearing efficiency of these three methods, we recorded the transparency, deformation, and pigmentation and compared the gross lens diameter after PFA fixation and after clearing. As shown in **Figure 2A**, the younger the lens, the more transparent it was after being isolated. The lens turned opaque after PFA fixation, and this could be reversed by our optical clearing methods. As far as the transparency was concerned, there was not much difference among the three methods. However, e-CLARITY seemed to cause a slight deformation of the lens, while CUBIC and iDISCO caused a small amount of pigmentation. Although the process of fixation and clearing could cause a certain degree of swelling or shrinkage when comparing the post-clearing to original diameter of the lens, both CUBIC and iDISCO showed no significant difference while e-CLARITY underwent severe expansion by about 150% (**Figure 2B**).

Basic parameter measurements of the lens after 3D reconstruction

To explore the basic measurement efficacy of our lens-clearing methods, we first analyzed the gross geometric measures and compared them with other methods, including OCT and digital shadow photogrammetry. Based on the even expansion and calibration of the 3D reconstruction, we could calculate several 3D parameters and could perform further micro-level analyses. Seven semi-automatically calculated parameters regarding thickness, diameter, and volume are shown in **Table 1**. Due to the high spatial resolution of the reconstruction, the sub-structure of the lens could be determined, including the equatorial region. Most of the parameters increased with age except for the equatorial proportion, which

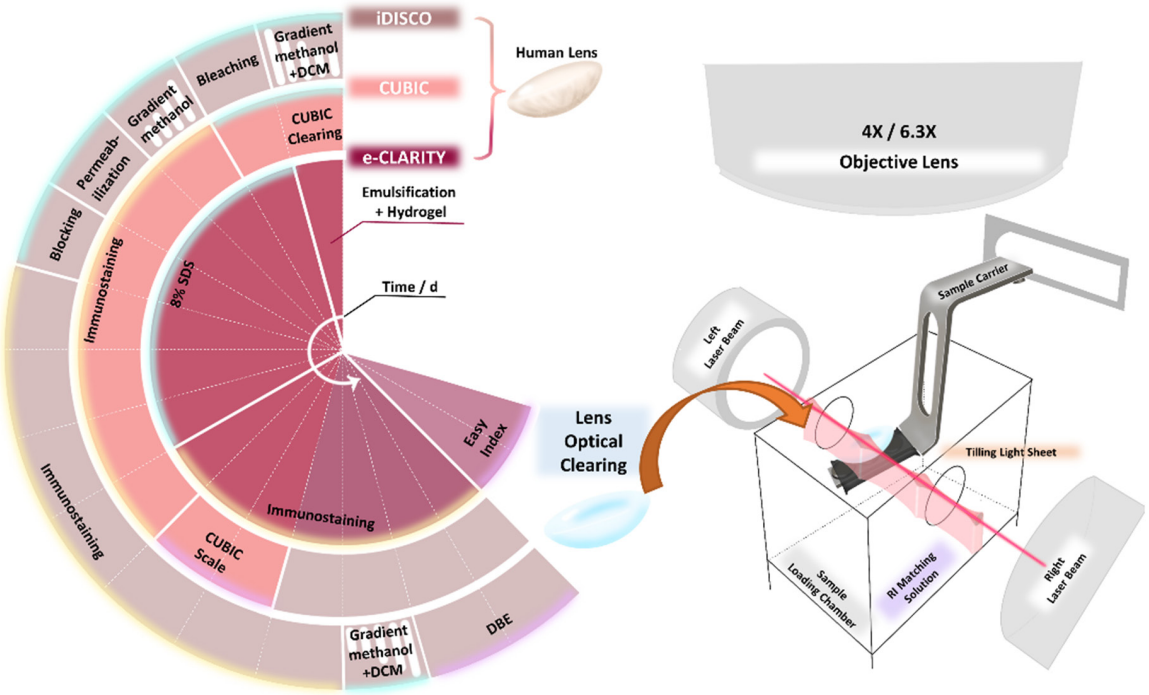

Figure 1. Timeline for the e-CLARITY, CUBIC, and iDISCO processes. The overview of the timeline and main reagents for e-CLARITY, CUBIC, and iDISCO. One sector represents one day, so the total processing time for each method was 17, 11, and 15 days, respectively. Each method consisted of clearing (blue highlight), immunostaining (yellow highlight), and refractive index matching (purple highlight) to achieve optical clearing, followed by versatile tiling light sheet imaging.

remained constant at 23.05% ± 0.36%. When compared to other methods such as OCT and digital shadow photogrammetry, most of the parameters calculated by lens-clearing methods fit well with the other two methods [32, 34], including lens thickness, equatorial diameter, and lens column, thus supporting the feasibility of our method.

3D map of cellular changes across different ages

In order to further explore the 3D cellular architecture of the lens, we traced the cellular changes in the lens during aging by reconstructing and analyzing the nuclear signal. The nuclei of all lens cells were stained by DAPI in the iDISCO method and by PI in the CUBIC method (**Figure 3A**, **3B**), and the equatorial region was segmented based on the morphology characterized by the largest diameter in the coronal plane together with the equatorial front part that was defined as the anterior capsule region (Supplementary Figure 2B). In addition, the cortex region was defined as the subepithelial part. From a 3D view, the lens cells could be roughly divided into three parts according to their spatial position, including the anterior capsular epithelium, the equatorial epithelium, and cortical fiber cells. Some parts of the anterior capsule were peeled off, possibly due to the shaking during the clearing process. All three groups of cells grew along with the age-increasing diameter of the lens, especially from the 6 M to the 17 Y lenses (**Figure 3A**, **3B**). In addition, the density of the equatorial epithelium reached its peak in the 17 Y lens. Interestingly, we found that the cortical fiber cells gathered together to form an inner ring just beneath the epithelium in the 6 M lens, and scattered in 17 Y and 49 Y lenses (**Figure 3A**, **3B**). Finally, in the 72 Y lens half of the lens had lost the cortical fiber cell nuclei (**Figure 3A**, **3B**).

Furthermore, we divided the lens into quarters to reduce sampling errors in the statistical analyses (Supplementary Figure 1B). Nuclei were reconstructed automatically using the Imaris *spots* item, as shown by the correlation between the reconstructed pink spots and the PI immunostained nuclei. Based on the quar-

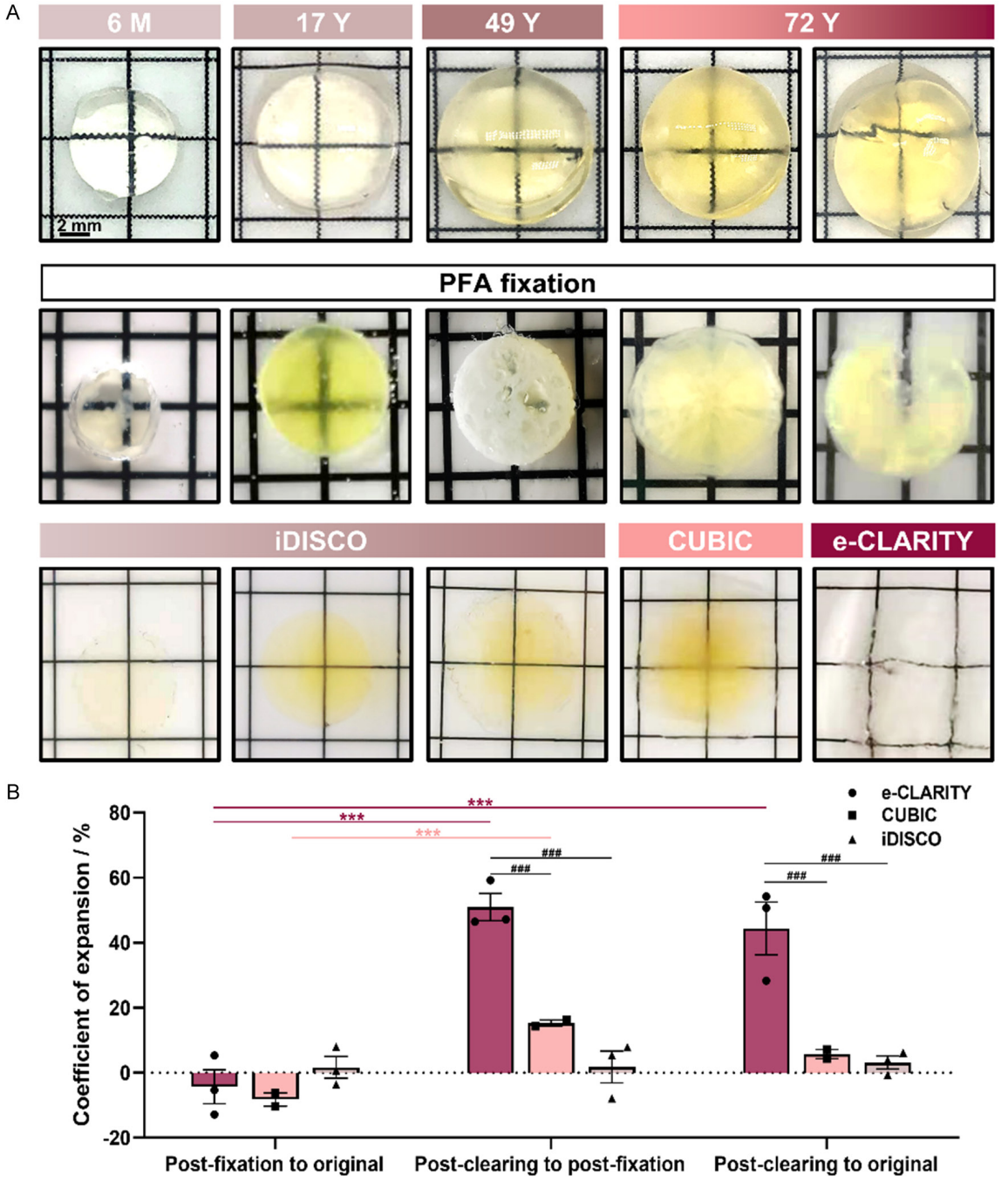

Figure 2. Human lens clearing efficacy of e-CLARITY, CUBIC, and iDISCO. A. The gross morphology of randomly-chosen lenses immediately after isolation (the top panel), after PFA fixation (the middle panel), and after clearing (the bottom panel), roughly showing the changes in size and degree of transparency. B. The coefficient of expansion of the three clearing methods after fixation and after clearing and as compared to the original. n = 3/group, ***P < 0.001 comparing within one method under different conditions; ###P < 0.001 comparing among the different methods under the same conditions.

tered lens, four points were referred to as 3, 6, 9, and 12 o'clock located where the split line intersected with the edge of the lens. We quantified the number of nuclei, the surface area, and the sphericity of the anterior capsule and equator and the centroid distance between the nucleus and the capsule (**Figure 3C-F**). The number of nuclei in all three groups and the

Table 1. Comparison of basic gross geometric parameters between the lens clearing methods and OCT and digital shadow photogrammetry

Geometric parameter	Lens optical clearing methods in this experiment				OCT [32]	Digital shadow Photogrammetry [34]
	6 M	17 Y	49 Y	72 Y	0-56 Y	0-88 Y
LT (mm)	3.6	3.7	4.3	4.1	3.5-5.5	3.0-6.0
ET (mm)	0.84	0.84	1.01	0.93	NA	NA
EP (%)	23.33%	22.70%	23.49%	22.68%	NA	NA
DIA (mm)	7.3	9.2	9.3	11.0[a]	5.5-10.0	6.0-11.0
EPP (mm)	1.12[a]	1.68	1.67	1.98	1.4-2.5	NA
LSA (mm^2)	113	177	247[a]	265[a]	80-200	NA
VOL (mm^3)	93	158	250	294[a]	50-250	NA

[a]Beyond the estimated range of OCT. LT, lens thickness; ET, equatorial thickness; EP, equatorial percentage; DIA, lens equatorial diameter; EPP, equatorial plane position; LSA, lens surface area; VOL, lens volume; NA, not applicable.

areas of the anterior capsule and equator changed significantly with age along with the centroid distance between the equatorial epithelium and the lens surface, especially from 6 M to 17 Y. In contrast, the centroid distance between the anterior capsular epithelium and cortical fiber cells and the lens surface, together with the sphericity, showed no significant differences among the different ages. Notably, the large decrease in anterior capsular epithelium and cortical cells (41.59% and 91.09%) occurred along with a large increase in the equatorial epithelium (150.70%), which resulted in a decrease in the total number of lens cells when reaching adolescence (**Figure 3C**).

Spatial distribution of ZO-1 in lens across different ages

To further understand the intercellular adhesion between lens cells, we determined the expression of ZO-1 in the 17 Y and 49 Y lenses (**Figure 4A**, **4B**). ZO-1 was mainly distributed at the interface between the capsule and epithelium fibers together with some expression in the cortical fiber cells extending from the anterior capsule to the frontal portion of the posterior capsule. Focusing on its distribution in the posterior capsule, ZO-1 in the 17 Y lens extended farther than in the 49 Y lens (**Figure 4a**, **4b**, Supplementary Figure 2C), and ZO-1 covered 66.7% of the frontal part of posterior capsule in the 17 Y lens but only 22.2% of the frontal part in the 49 Y lens. In both the 17 Y and 49 Y lenses the expression of ZO-1 in the direction of 3, 6, 9, and 12 o'clock grew thicker from the central to the peripheral zone beneath the anterior capsule and peaked just before the equatorial region, while it gradually became thinner beneath the posterior capsule. The maximum thickness of the ZO-1 signal in the 17 Y and 49 Y lenses was 30.67 ± 3.7 μm and 38.40 ± 5.94 μm, respectively, while the thickness of the nuclei was 41.58 ± 3.62 μm and 51.70 ± 12.74 μm, respectively. In addition, DAPI marked the epithelium and denucleated fiber cells closely surrounding the cells expressing ZO-1 and showed a similar pattern as ZO-1 expression (**Figure 4C**, **4D**). We also observed the changing thickness of DAPI and TrkA in the 6 M lens (**Figure 4e**) and found a similar pattern as ZO-1 in the 17 Y and 49 Y lenses, except that TrkA reached its thickest point just behind the equator (**Figure 4E**, **4F**, Supplementary Figure 2D). Furthermore, we reduced the interval between the measuring planes to about 20 μm for the equatorial observation, and DAPI, TrkA, and ZO-1 all showed a slight decline from the front to the back in all lenses (**Figure 4G**, **4H**). A similar pattern between TrkA, ZO-1, and DAPI from the anterior to the posterior indicated the close relationship between ZO-1, TrkA, and the epithelium. The slight decrease in ZO-1 and DAPI signals within the equatorial region indicated that ZO-1 in the anterior capsule peaked before the equator (**Figure 4G**, **4H**). When comparing the three age groups, it was observed that the younger the lens, the thinner the capsule within the equatorial region (**Figure 4H**).

Discussion

The human lens is a highly organized structure that remains transparent throughout the lifetime, and understanding its spatial cellular and molecular features will improve our ability to

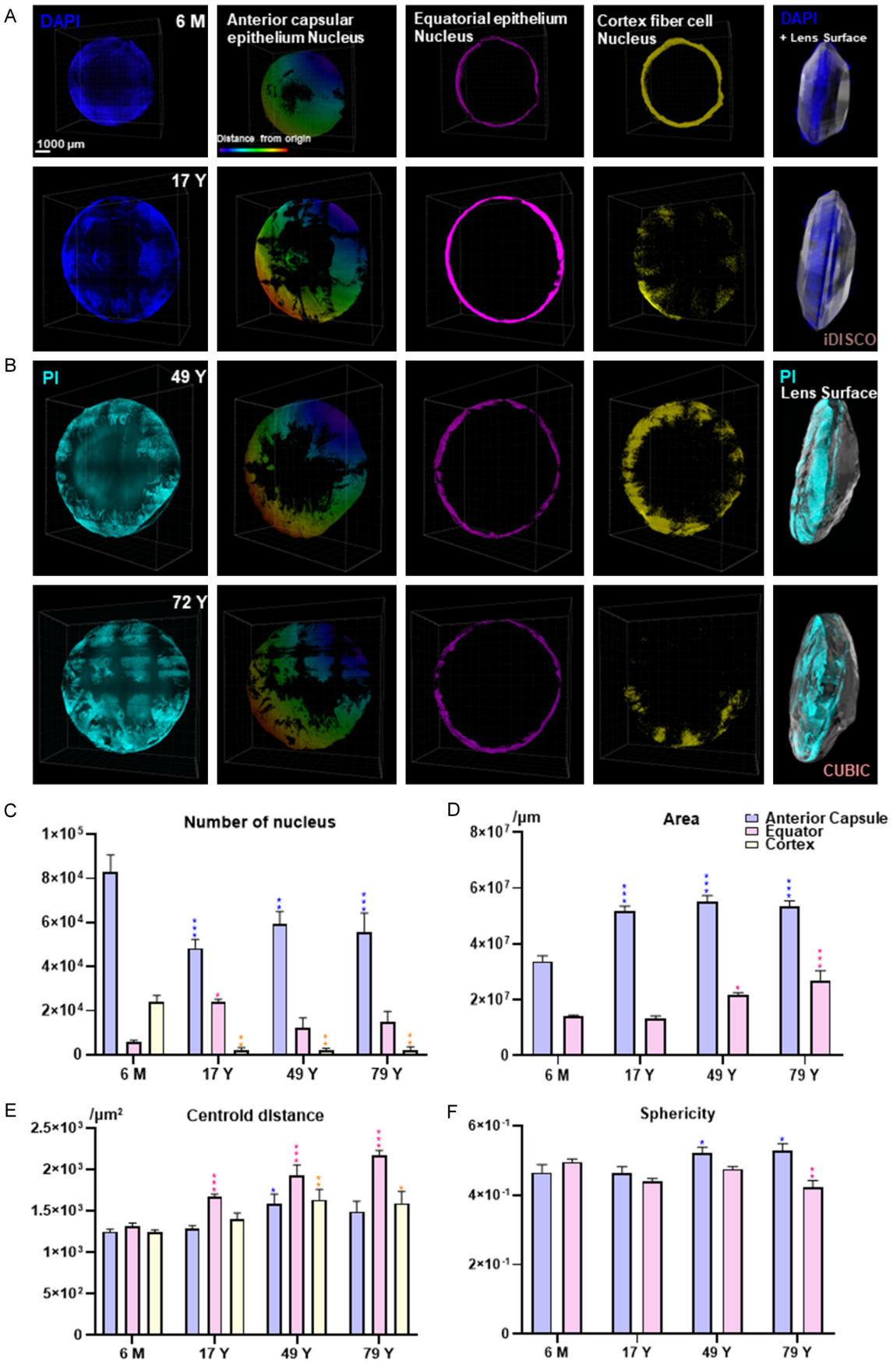
A
DAPI
6 M
1000 μm
Anterior capsular epithelium Nucleus
Distance from origin
Equatorial epithelium Nucleus
Cortex fiber cell Nucleus
DAPI
+ Lens Surface
17 Y
iDISCO
B
PI
49 Y
PI
Lens Surface
72 Y
CUBIC
C
Number of nucleus
1×10^5
8×10^4
6×10^4
4×10^4
2×10^4
0
6 M
17 Y
49 Y
79 Y
D
/μm
Area
Anterior Capsule
Equator
Cortex
8×10^7
6×10^7
4×10^7
2×10^7
0
6 M
17 Y
49 Y
79 Y
E
/μm²
Centrold distance
2.5×10^3
2×10^3
1.5×10^3
1×10^3
5×10^2
0
6 M
17 Y
49 Y
79 Y
F
Sphericity
6×10^-1
4×10^-1
2×10^-1
0
6 M
17 Y
49 Y
79 Y

Figure 3. 3D cellular maps of the human lens across different ages. 3D cellular maps of (A) 6 M and 17 Y lenses stained by DAPI (dark blue) and (B) 49 Y and 72 Y lenses stained by PI (light blue). The first four columns show the frontal view, including the original signal, the reconstructed anterior capsular epithelium, the equatorial epithelium, and the cortical fiber cells. Among these, in the second column the color represents the distance from the origin with red being farther away and purple being closer. The last column shows the side view of the original signal. (C-F) Cellular 3D parameters are shown as a statistical graph comparing the different ages and different lens parameters, including the number of nuclei, the area, the centroid distance, and the sphericity. Data for the 6 M and 17 Y lenses were obtained using iDISCO, and data for 49 Y and 72 Y lenses were obtained using CUBIC. n = 4/group, *P < 0.05, **P < 0.01, ***P < 0.001 compared to the 6 M lens.

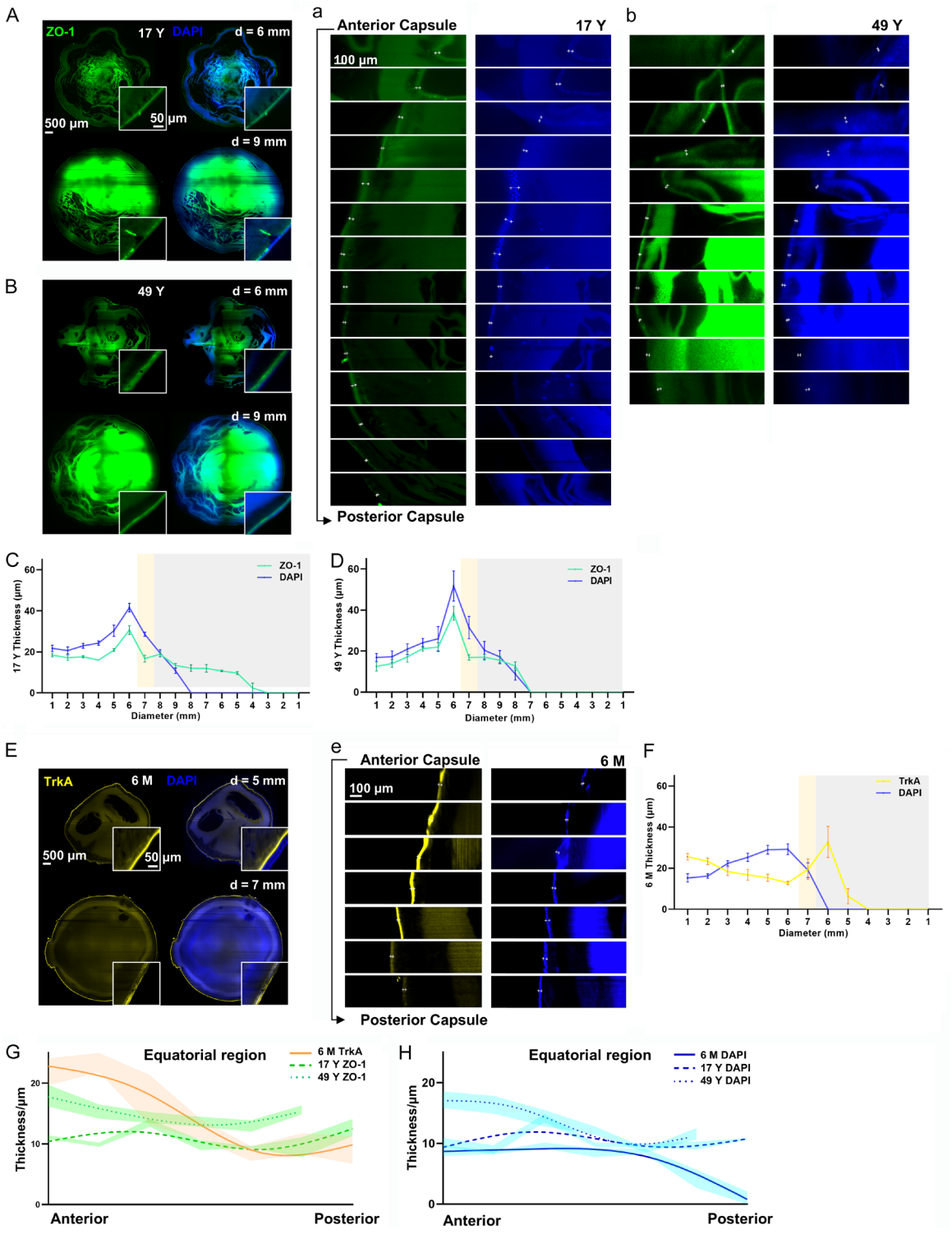

Figure 4. 3D distribution of ZO-1 and TrkA in the whole human lens. Representative images of the anterior coronal plane at a diameter of 6 mm and 9 mm showing ZO-1 (green) and DAPI (blue) in (A) the 17 Y lens and (B) the 49 Y lens, with continuous thickness changes being repeatedly calculated at 3, 6, 9, and 12 o'clock from the anterior to posterior of the lens (white, yellow, and gray represent the anterior capsule, equator, and posterior capsule region, respectively) in (C) the 17 Y lens and (D) the 49 Y lens. Representative continuous imaging from the anterior to posterior (with a measuring plane interval of 1 mm) of ZO-1 and DAPI at 9 o'clock is shown for (a) the 17 Y lens and (b) the 49 Y lens. (E) Representative images of the anterior coronal plane at diameters of 5 mm and 7 mm showing TrkA (nerve growth factor receptor, yellow) and DAPI (nucleus, blue) in the 6 M lens. (F) Continuous thickness changes of TrkA (yellow) and DAPI (blue) were repeatedly calculated at 3, 6, 9, and 12 o'clock from the anterior to posterior (white, yellow, and gray represent the anterior capsule, equator, and posterior capsule, respectively) as shown in the 6 M lens. (e) Representative continuous imaging from the anterior capsule to the posterior (with a measuring plane interval of 1 mm) of TrkA and DAPI at 9 o'clock in the 6 M lens. Furthermore, fit spline analyses of (G) ZO-1 (green) and TrkA (orange) and (H) DAPI (blue) are shown within the equator from the anterior to posterior (with a measuring plane interval of 20 μm). n = 4/group.

restore transparency under pathologic conditions. Our study first optimized three different methods to clear the human lens in terms of the time required and the labeling efficiency. Through 3D reconstruction and statistical analysis of the nuclear distribution within the capsule, equator, and cortex, we could observe the cellular and molecular characteristics of the whole lens. ZO-1 and TrkA had similar distribution patterns as the epithelium, indicating their close relationship.

Tissue clearing methods have recently been developed and widely applied in studies of various organs, and these methods mainly consist of clearing, immunostaining, and microscope imaging procedures [16, 35]. All of the techniques have primarily benefitted from advances in microscopy resulting in high-speed image acquisition and minimal photobleaching together with the big data computing and analysis systems that are necessary for terabyte-level image reconstructions and calculations [36, 37]. The biggest breakthrough in tissue clearing methods was by no means just the 3D visualization, but also the ability for 3D reconstruction, quantification, and modeling [38-40]. Although there are numerous mature clinical optical examination techniques such as OCT, Purkinje imaging, Scheimpflug imaging, and digital shadow photogrammetry [34, 41-43], as well as non-optical techniques such as X-ray Talbot interferometry, magnetic resonance imaging, and ultrasound biomicroscopy [44-46], their inability to support in-depth micro-level exploration limits their usefulness in understanding the micro-world buried beneath the opaque tissue. Thus, tissue clearing methods have been developed to make up for these clinical shortcomings and to more deeply explore the components of the lens.

Comparing the three different kinds of clearing methods, we found iDISCO to be the most suitable for the clearing and immunostaining of the human lens. We first applied the traditional CLARITY method based on our previous experience [24]. However, due to the weaker water absorption and expansion capacity of the capsule compared with fibers, together with the intensified expansion due to the long SDS clearing process (about 7 days), the lens tended to burst easily during the SDS clearing step (data not shown). Thus, in order to balance the inner pressure caused by fibers and the outer pressure caused by the capsule, we added the enucleation step before embedding in SDS. We modified the e-CLARITY procedure to include splitting the posterior capsule and sucking out part of the nucleus of the lens in order to balance the internal and external pressure. Our e-CLARITY data showed a great enlargement of the sample, indicating its potential use in magnifying and detecting more delicate structures, theoretically similar to the Magnified Analysis of the Proteome technique [47, 48]. Nevertheless, the splitting of the posterior capsule and enucleation of the nucleus destroys the integrity of the lens. To avoid swelling of the tissue, we next tried the organic clearing methods CUBIC and iDISCO. In the CUBIC process, we added the PI directly with the CUBIC clearing solution in order to reduce the immunostaining time, and in iDISCO we modified the antibody incubation time. Adding PI to the CUBIC clearing solution allowed us to skip the washing step for the immunostaining. iDISCO has a penetration step, so we reduced the staining time based on our lens samples as appropriate. Both PI and DAPI can bind to DNA, the only difference being the lack of cell membrane penetrability for PI [49, 50]. Owing to the membrane

penetration treatment in the whole clearing process, the entire lens nucleus could be stained. Both the CUBIC and iDISCO methods performed well in the human lens, except for slightly better transparency with the iDISCO method. Due to the specific penetration step, iDISCO was also more appropriate for immunostaining using a wide range of different markers.

Our methods could determine not only the parameters that are already being applied in clinical practice, but also several other 3D cellular parameters. In addition to well-accepted parameters like lens thickness, lens volume, lens equatorial diameter, and the radius of the curvature of the lens [32, 34, 42, 44, 51], we also defined the equatorial thickness and the equatorial proportion. We observed a constant equatorial proportion of around 22-23% in both young and aged lenses, but whether this value might change under pathologic conditions needs further clinical investigations. Moreover, the previously reported slight variation in the ratio of the equatorial height to the lens thickness across different ages, which agrees with our finding of a constant equatorial proportion [52].

We also reconstructed the position of each lens cell together with the capsule morphology to support the cell development theory of the lens. The human crystalline lens has a high degree of spatiotemporally organized tissue [53], and an increase in mass and a flattening of the anterior capsular curvature occurs during aging together with increased light scattering and spectral absorption [54]. It is believed that the anterior capsule is the only metabolically active part of the lens, with the germinative zone located just pre-equatorially where cells undergo mitosis, migrate towards the equator, and differentiate into fiber cells [55]. The newly-differentiated fiber cells elongate and become densely packed surrounding the older fiber cells, and they show upregulated expression of α-, β-, and γ-crystallins along with degradation of their nuclei and organelles, thus maintaining the continuous growth and transparency of the lens [56, 57].

With regards to changes in the number of lens cells across different ages in our experiment, the following distribution patterns were observed: 1) the anterior capsular epithelium in the 6 M lens was almost one-and-a-half times as thick as in the 72 Y lens, and the number of cortical fiber cells was almost 10 times greater, 2) the accumulation of equatorial epithelium peaked at around 17 Y, and 3) there was a slight decrease in the total number of cells in the whole lens and an increase in the number of cortical cells in the elder sample. Our results for lens cell numbers and spatiotemporal distributions from different ages (Supplementary Video 1) suggest that the infant lens is rich in cells in the anterior capsular epithelium and equatorial epithelium, especially denucleated cortical fiber cells. In the progression to adolescence, many epithelial cells in the germinative zone underwent mitosis and migrated to the equator, but only a relatively small part of the equatorial epithelium denucleated and packed into the cortex, which could explain the intense increase in equatorial epithelium and the decrease in the anterior capsular epithelium and the decrease in cortical fiber cells.

Another aspect of our study focused on ZO-1, which is associated with tight junctions and is mainly located at the epithelium-fiber interface [58]. In addition, ZO-1 can interact with various proteins and can reorganize the membrane domain and signaling pathways and thus plays a role in various cataract-related pathologic conditions like Nance-Horan syndrome [59, 60]. In our experiment, ZO-1 was mainly distributed at the epithelium-fiber interface (Supplementary Video 2). In our continuous observation of ZO-1 from the front to the back of the lens, we found that in both the adolescent and middle-aged lenses the expression of ZO-1 reached its maximum just before the equator, together with the densest nuclei, indicating the location of the germinative zone. Moreover, both the epithelium and ZO-1 became thicker in the older lenses. Another interesting thing about ZO-1 was that in the 17 Y lens ZO-1 expression extended farther towards the posterior capsule than the epithelium, partially due to the incomplete packing process of denucleated cortical fiber cells. TrkA expression in the 6 M lens followed a similar pattern and might also be partially explained by the incomplete denucleated packing process. The lack of overlap of ZO-1 and TrkA with the epithelium is an indication of the immature lens cortex during early life. Because TrkA is the receptor for nerve growth factor [61], its distribution as shown here suggests a role in the trophism

and growth of the epithelium, and this needs further study at the molecular level.

There are several limitations to this study. First, due to the need to obtain fresh lenses without freezing from healthy individuals without ocular diseases, which is a rarity in young and middle-aged populations, this research is constrained by a limited sample size and lack of young subjects. We specifically selected lenses representing infancy (6 months), adolescence (17 years), middle age (49 years), and the elderly (72 years). Additionally, due to our sample size limitations, staining of TrkA and ZO-1 was not performed in the aged lenses. Finally, the fibrous tissue might still cause light scattering even when it looks transparent to the naked eye, and an additional quenching step might be applied to avoid false-positive signals.

Conclusion

The three modified tissue clearing methods of e-CLARITY, CUBIC, and iDISCO were successfully applied to the human lens. Subsequent 3D cellular reconstruction revealed the cellular and molecular characteristics in the human lens across different ages together with the molecular distribution of ZO-1 and TrkA.

Acknowledgements

For image analyses, the authors thank Dr. Yi Feng's lab for the tissue clearing process, light-sheet microscopy imaging, figures, and movie editing as well as the Core Facility for Large-Scale Tissue Clearing and Data Analysis of Department of Integrative Medicine and Neurobiology, School of Basic Medical Sciences, Fudan University. This work was supported by the National Natural Science Foundation of China (NSFC 81670840 to J.L. and NSFC 81973945 & 81673766 to Y.F.), the Innovative Research Team of High-level Local Universities in Shanghai, the Development Project of Shanghai Peak Disciplines-Integrated Chinese and Western Medicine (20180101), and the Project Supported by Shanghai Municipal Science and Technology Major Project (No. 2018SHZDZX01) and ZJlab.

Disclosure of conflict of interest

None.

Address correspondence to: Dr. Jin Li, Eye Hospital of Wenzhou Medical University, 270 West Xueyuan Road, Wenzhou 325027, Zhejiang, China. Tel: +86-0577-88068876; Fax: +86-0577-88832083; E-mail: lijin_wz@eye.ac.cn; Dr. Yi Feng, Department of Integrative Medicine and Neurobiology, School of Basic Medical Sciences, Institutes of Brain Science, Brain Science Collaborative Innovation Center, State Key Laboratory of Medical Neurobiology, Institute of Acupuncture and Moxibustion, Fudan Institutes of Integrative Medicine, Fudan University, P.O. Box 291, 138 Yi-Xue-Yuan Road, Shanghai 200032, China. Tel: +86-21-54237693; Fax: +86-21-54237526; E-mail: fengyi17@fudan.edu.cn

References

[1] Hejtmancik JF and Shiels A. Overview of the Lens. Prog Mol Biol Transl Sci 2015; 134: 119-127.
[2] Glasser A and Campbell MC. Presbyopia and the optical changes in the human crystalline lens with age. Vision Res 1998; 38: 209-229.
[3] Akella SS and Juthani VV. Extended depth of focus intraocular lenses for presbyopia. Curr Opin Ophthalmol 2018; 29: 318-322.
[4] Harding JJ and Dilley KJ. Structural proteins of the mammalian lens: a review with emphasis on changes in development, aging and cataract. Exp Eye Res 1976; 22: 1-73.
[5] Fernández J, Sánchez-García A, Rodríguez-Vallejo M and Piñero DP. Systematic review of potential causes of intraocular lens opacification. Clin Exp Ophthalmol 2020; 48: 89-97.
[6] Augusteyn RC. Growth of the eye lens: I. Weight accumulation in multiple species. Mol Vis 2014; 20: 410-426.
[7] Aspects of transparency in the lens. Acta Ophthalmologica 1969; 47: 5-9.
[8] Beebe DC. Maintaining transparency: a review of the developmental physiology and pathophysiology of two avascular tissues. Semin Cell Dev Biol 2008; 19: 125-133.
[9] Al-Ghoul KJ, Kuszak JR, Lu JY and Owens MJ. Morphology and organization of posterior fiber ends during migration. Mol Vis 2003; 9: 119-128.
[10] Kwon C, Kim Y and Jeon H. Collective migration of lens epithelial cell induced by differential microscale groove patterns. J Funct Biomater 2017; 8: 34.
[11] Martinez-Enriquez E, Sun M, Velasco-Ocana M, Birkenfeld J, Pérez-Merino P and Marcos S. Optical coherence tomography based estimates of crystalline lens volume, equatorial diameter, and plane position. Invest Ophthalmol Vis Sci 2016; 57: OCT600-10.
[12] Singh KD, Logan NS and Gilmartin B. Three-dimensional modeling of the human eye based on magnetic resonance imaging. Invest Ophthalmol Vis Sci 2006; 47: 2272-2279.

[13] Wu JJ, Wu W, Tholozan FM, Saunter CD, Girkin JM and Quinlan RA. A dimensionless ordered pull-through model of the mammalian lens epithelium evidences scaling across species and explains the age-dependent changes in cell density in the human lens. J R Soc Interface 2015; 12: 20150391.
[14] Brown N and Bron AJ. An estimate of the human lens epithelial cell size in vivo. Exp Eye Res 1987; 44: 899-906.
[15] Tian T, Yang Z and Li X. Tissue clearing technique: recent progress and biomedical applications. J Anat 2021; 238: 489-507.
[16] Ueda HR, Ertürk A, Chung K, Gradinaru V, Chédotal A, Tomancak P and Keller PJ. Tissue clearing and its applications in neuroscience. Nat Rev Neurosci 2020; 21: 61-79.
[17] Prieto-Bonete G, Perez-Carceles MD and Luna A. Morphological and histological changes in eye lens: possible application for estimating postmortem interval. Leg Med (Tokyo) 2015; 17: 437-442.
[18] Yang Y, Li G and Chen L. High resolution three-dimensional imaging of the ocular surface and intact eyeball using tissue clearing and light sheet microscopy. Ocul Surf 2020; 18: 526-532.
[19] Ye Y, Dinh Duong TA, Saito K, Shinmyo Y, Ichikawa Y, Higashide T, Kagami K, Fujiwara H, Sugiyama K and Kawasaki H. Visualization of the retina in intact eyes of mice and ferrets using a tissue clearing method. Transl Vis Sci Technol 2020; 9: 1.
[20] Henning Y, Osadnik C and Malkemper EP. Eye-Ci: optical clearing and imaging of immunolabeled mouse eyes using light-sheet fluorescence microscopy. Exp Eye Res 2019; 180: 137-145.
[21] Danysh BP and Duncan MK. The lens capsule. Exp Eye Res 2009; 88: 151-164.
[22] Lin L, Lin Q, Li J, Han Y, Chang P, Lu F and Zhao YE. ROCK inhibitor modified intraocular lens as an approach for inhibiting the proliferation and migration of lens epithelial cells and posterior capsule opacification. Biomater Sci 2019; 7: 4208-4217.
[23] Hennig A, Kumar J, Yorston D and Foster A. Sutureless cataract surgery with nucleus extraction: outcome of a prospective study in Nepal. Br J Ophthalmol 2003; 87: 266-270.
[24] Chung K and Deisseroth K. CLARITY for mapping the nervous system. Nat Methods 2013; 10: 508-513.
[25] Feng Y, Cui P, Lu X, Hsueh B, Möller Billig F, Zarnescu Yanez L, Tomer R, Boerboom D, Carmeliet P, Deisseroth K and Hsueh AJ. CLARITY reveals dynamics of ovarian follicular architecture and vasculature in three-dimensions. Sci Rep 2017; 7: 44810.
[26] Hu W, Tamadon A, Hsueh AJW and Feng Y. Three-dimensional reconstruction of the vascular architecture of the passive CLARITY-cleared mouse ovary. J Vis Exp 2017; 56141.
[27] Susaki EA, Tainaka K, Perrin D, Yukinaga H, Kuno A and Ueda HR. Advanced CUBIC protocols for whole-brain and whole-body clearing and imaging. Nat Protoc 2015; 10: 1709-1727.
[28] Tong X, Liu Y, Xu X, Shi J, Hu W, Ma T, Cui P, Lu W, Pei Z, Xu M, Zhang F, Li X and Feng Y. Ovarian innervation coupling with vascularity: the role of electro-acupuncture in follicular maturation in a rat model of polycystic ovary syndrome. Front Physiol 2020; 11: 474.
[29] Hu W, Chen J, Sun C, Tong X, Lu W, Ju Z, Xia Y, Pei Z, Xu M, Xu X, Shi J, Li Y, Chen H, Lu Y, Ying Y, Gao H, Hsueh AJW, Zhang F, Lü Z and Feng Y. Spatial topological analysis of sympathetic neurovascular characteristic of acupoints in Ren meridian using advanced tissue-clearing and near infrared II imaging. Comput Struct Biotechnol J 2021; 19: 2236-2245.
[30] Renier N, Wu Z, Simon DJ, Yang J, Ariel P and Tessier-Lavigne M. iDISCO: a simple, rapid method to immunolabel large tissue samples for volume imaging. Cell 2014; 159: 896-910.
[31] Chen Y, Li X, Zhang D, Wang C, Feng R, Li X, Wen Y, Xu H, Zhang XS, Yang X, Chen Y, Feng Y, Zhou B, Chen BC, Lei K, Cai S, Jia JM and Gao L. A versatile tiling light sheet microscope for imaging of cleared tissues. Cell Rep 2020; 33: 108349.
[32] Martinez-Enriquez E, de Castro A, Mohamed A, Sravani NG, Ruggeri M, Manns F and Marcos S. Age-related changes to the three-dimensional full shape of the isolated human crystalline lens. Invest Ophthalmol Vis Sci 2020; 61: 11.
[33] Cruz-Matías I, Ayala D, Hiller D, Gutsch S, Zacharias M, Estradé S and Peiró F. Sphericity and roundness computation for particles using the extreme vertices model. J Comput Sci 2019; 30: 28-40.
[34] Mohamed A, Durkee HA, Williams S, Manns F, Ho A, Parel JA and Augusteyn RC. Morphometric analysis of in vitro human crystalline lenses using digital shadow photogrammetry. Exp Eye Res 2021; 202: 108334.
[35] Richardson DS and Lichtman JW. Clarifying tissue clearing. Cell 2015; 162: 246-257.
[36] Wan Y, McDole K and Keller PJ. Light-sheet microscopy and its potential for understanding developmental processes. Annu Rev Cell Dev Biol 2019; 35: 655-681.
[37] Fetit A. Big data and bio-image informatics. Standard and super-resolution bioimaging data analysis. 2017. pp. 227-248.
[38] Elisa Z, Toon B, De Smedt SC, Katrien R, Kristiaan N and Kevin B. Technical implementa-

tions of light sheet microscopy. Microsc Res Tech 2018; 81: 941-958.
[39] França CM, Riggers R, Muschler JL, Widbiller M, Lococo PM, Diogenes A and Bertassoni LE. 3D-imaging of whole neuronal and vascular networks of the human dental pulp via CLARITY and light sheet microscopy. Sci Rep 2019; 9: 10860.
[40] Hu W, Chen J, Sun C, Tong X, Lu W, Ju Z, Xia Y, Pei Z, Xu M, Xu X, Shi J, Li Y, Chen H, Lu Y, Ying Y, Gao H, Hsueh AJW, Zhang F, Lü Z and Feng Y. Spatial topological analysis of sympathetic neurovascular characteristic of acupoints in Ren meridian using advanced tissue-clearing and near infrared II imaging. Comput Struct Biotechnol J 2021; 19: 2236-2245.
[41] Ramos JL, Li Y and Huang D. Clinical and research applications of anterior segment optical coherence tomography - a review. Clin Exp Ophthalmol 2009; 37: 81-89.
[42] Rosales P, Dubbelman M, Marcos S and van der Heijde R. Crystalline lens radii of curvature from Purkinje and Scheimpflug imaging. J Vis 2006; 6: 1057-1067.
[43] Koretz JF, Cook CA and Kaufman PL. Aging of the human lens: changes in lens shape at zero-diopter accommodation. J Opt Soc Am A Opt Image Sci Vis 2001; 18: 265-272.
[44] Bahrami M, Hoshino M, Pierscionek B, Yagi N, Regini J and Uesugi K. Refractive index degeneration in older lenses: a potential functional correlate to structural changes that underlie cataract formation. Exp Eye Res 2015; 140: 19-27.
[45] Rozema JJ, Atchison DA, Kasthurirangan S, Pope JM and Tassignon MJ. Methods to estimate the size and shape of the unaccommodated crystalline lens in vivo. Invest Ophthalmol Vis Sci 2012; 53: 2533-2540.
[46] Lie AL, Pan X, White TW, Donaldson PJ and Vaghefi E. Using the lens paradox to optimize an in vivo MRI-based optical model of the aging human crystalline lens. Transl Vis Sci Technol 2020; 9: 39.
[47] Ku T, Swaney J, Park JY, Albanese A, Murray E, Cho JH, Park YG, Mangena V, Chen J and Chung K. Multiplexed and scalable super-resolution imaging of three-dimensional protein localization in size-adjustable tissues. Nat Biotechnol 2016; 34: 973-981.
[48] Woo J, Seo JM, Lee M, Kim J, Min S, Kim ST, Ku S and Park JY. A modified magnified analysis of proteome (MAP) method for super-resolution cell imaging that retains fluorescence. Sci Rep 2020; 10: 4186.
[49] Yeh CJ, Hsi BL and Faulk WP. Propidium iodide as a nuclear marker in immunofluorescence. II. Use with cellular identification and viability studies. J Immunol Methods 1981; 43: 269-275.
[50] Kapuscinski J. DAPI: a DNA-specific fluorescent probe. Biotech Histochem 1995; 70: 220-233.
[51] Ruggeri M, Williams S, Heilman BM, Yao Y, Chang YC, Mohamed A, Sravani NG, Durkee H, Rowaan C, Gonzalez A, Ho A, Parel JM and Manns F. System for on- and off-axis volumetric OCT imaging and ray tracing aberrometry of the crystalline lens. Biomed Opt Express 2018; 9: 3834-3851.
[52] Pierscionek B, Bahrami M, Hoshino M, Uesugi K, Regini J and Yagi N. The eye lens: age-related trends and individual variations in refractive index and shape parameters. Oncotarget 2015; 6: 30532-30544.
[53] Cvekl A and Zhang X. Signaling and gene regulatory networks in mammalian lens development. Trends Genet 2017; 33: 677-702.
[54] Aliò JL, Anania A and Sagnelli P. The aging of the human lens. In: Cavallotti CAP and Cerulli L, editors. Age-related changes of the human eye. Totowa, NJ: Humana Press; 2008. pp. 61-131.
[55] Remington LA. Chapter 5 - crystalline lens. In: Remington LA, editors. Clinical anatomy and physiology of the visual system (Third Edition). Saint Louis: Butterworth-Heinemann; 2012. pp. 93-108.
[56] Petrash JM. Aging and age-related diseases of the ocular lens and vitreous body. Invest Ophthalmol Vis Sci 2013; 54: ORSF54-9.
[57] Bassnett S. On the mechanism of organelle degradation in the vertebrate lens. Exp Eye Res 2009; 88: 133-139.
[58] Dave A, Craig JE and Sharma S. The status of intercellular junctions in established lens epithelial cell lines. Mol Vis 2012; 18: 2937-2946.
[59] Nielsen PA, Baruch A, Shestopalov VI, Giepmans BN, Dunia I, Benedetti EL and Kumar NM. Lens connexins alpha3Cx46 and alpha8Cx50 interact with zonula occludens protein-1 (ZO-1). Mol Biol Cell 2003; 14: 2470-2481.
[60] Sharma S, Ang SL, Shaw M, Mackey DA, Gécz J, McAvoy JW and Craig JE. Nance-Horan syndrome protein, NHS, associates with epithelial cell junctions. Hum Mol Genet 2006; 15: 1972-1983.
[61] Ghinelli E, Aloe L, Cortes M, Micera A, Lambiase A and Bonini S. Nerve growth factor (NGF) and lenses: effects of NGF in an in vitro rat model of cataract. Graefes Arch Clin Exp Ophthalmol 2003; 241: 845-851.

Supplementary Table 1. Reagents, antibodies, equipment, and software

Name	Cat. number	Manufacturer
Reagent		
4% paraformaldehyde (PFA)	CR10010	Crystal-bio, China
PBS	C10010500BT	Gibco, USA
Triton X-100	V900502	Sigma-Aldrich, USA
Sodium azide	S2002	Sigma-Aldrich, USA
e-CLARITY		
Hydrogel solution		
Acrylamide	v900845	Vetec
Bisacrylamide	0172	Amresco
Photoinitiator VA044	va-044/225-02111	Wako
8% SDS solution		
Sodium dodecyl sulfate	30166428	Sinopharm Chemical Reagent
Boric acid	10004818	Sinopharm Chemical Reagent
Sodium hydroxide	10019718	Sinopharm Chemical Reagent
easyIndex	#EI-Z1011	LifeCanvas
CUBIC		
CUBIC clearing solution		
Urea	U5378	Sigma-Aldrich, USA
Tetraethylenediamine	101129	Crystal-bio, China
CUBIC scale solution		
Sucrose	CR101108	Crystal-bio, China
Triethanolamine	101109	Crystal-bio, China
Mineral oil	m8410	Sigma-Aldrich, USA
Silicone oil	TSF-437	Shanghai Puxian, China
iDISCO		
Methanol	34860	Sigma-Aldrich
DCM	270997	Sigma-Aldrich
H_2O_2	D216763	Sigma-Aldrich
Donkey serum	D9663	Sigma-Aldrich
PTwH		
Glycine	G8898	Sigma-Aldrich
DMSO	D8418	Sigma-Aldrich
Tween-20	P9416	Sigma-Aldrich
Heparin	375095	Milipore
Dibenzyl Ether	33630	Sigma-Aldrich
Antibodies		
DAPI	D9542	Sigma-Aldrich
PI	P1304MP	Thermo Fisher Scientific
TrKA	MA5-15509	Invitrogen
ZO-1	33-9100	Invitrogen
Equipment		
Constant temperature incubator	ZHLY-1803	Shanghai Zhichu Instrument, China
Light sheet microscope	LS-18	Nuohai Life Science Co., Ltd., China
Workstation	W-2245	Intel
Software		
Imaris	Imaris 9.7	Bitplane, Switzerland
MATLAB	R2016a	MathWorks, USA
GraphPad Prism	version 8.0.2	GraphPad

Supplementary Table 2. Tissue clearing and immunostaining methods for each individual lens

Sample	Tissue clearing method	Immunostaining methods
6 M	iDISCO	DAPI, TrkA
17 Y	iDISCO	DAPI, ZO-1
49 Y #1	CUBIC	PI
49 Y #2	iDISCO	DAPI, ZO-1
72 Y #1	CUBIC	PI
72 Y #2	e-CLARITY	DAPI

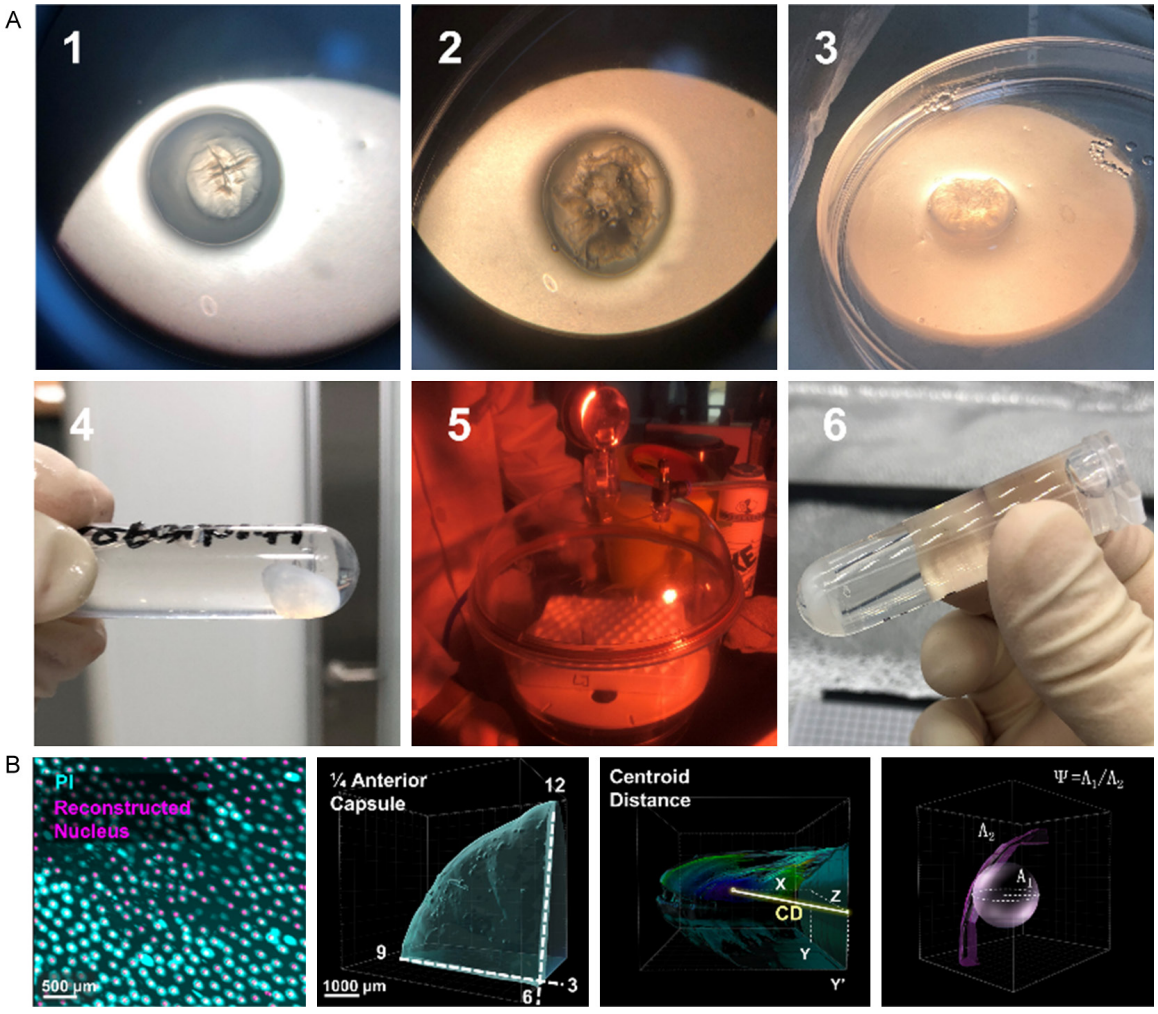

Supplementary Figure 1. Pretreatment with enucleation and subsequent e-CLARITY 3D-reconstruction. A. Pretreatment with enucleation in the e-CLARITY process. 1 - the isolated lens after removing the central 6 mm of the posterior capsule; 2 - the hollowed-out lens; 3 - the lens filled with hydrogel; 4 - sealing the lens in the Eppendorf tube with hydrogel; 5 - degassing with a vacuum desiccator; and 6 - solidified hydrogel containing the lens. B. Cellular 3D parameters are shown as a schematic diagram of definitions comparing the different ages and different lens parts, including the number of nuclei, the area, the centroid distance, and the sphericity.

3D mapping of human lenses across different ages

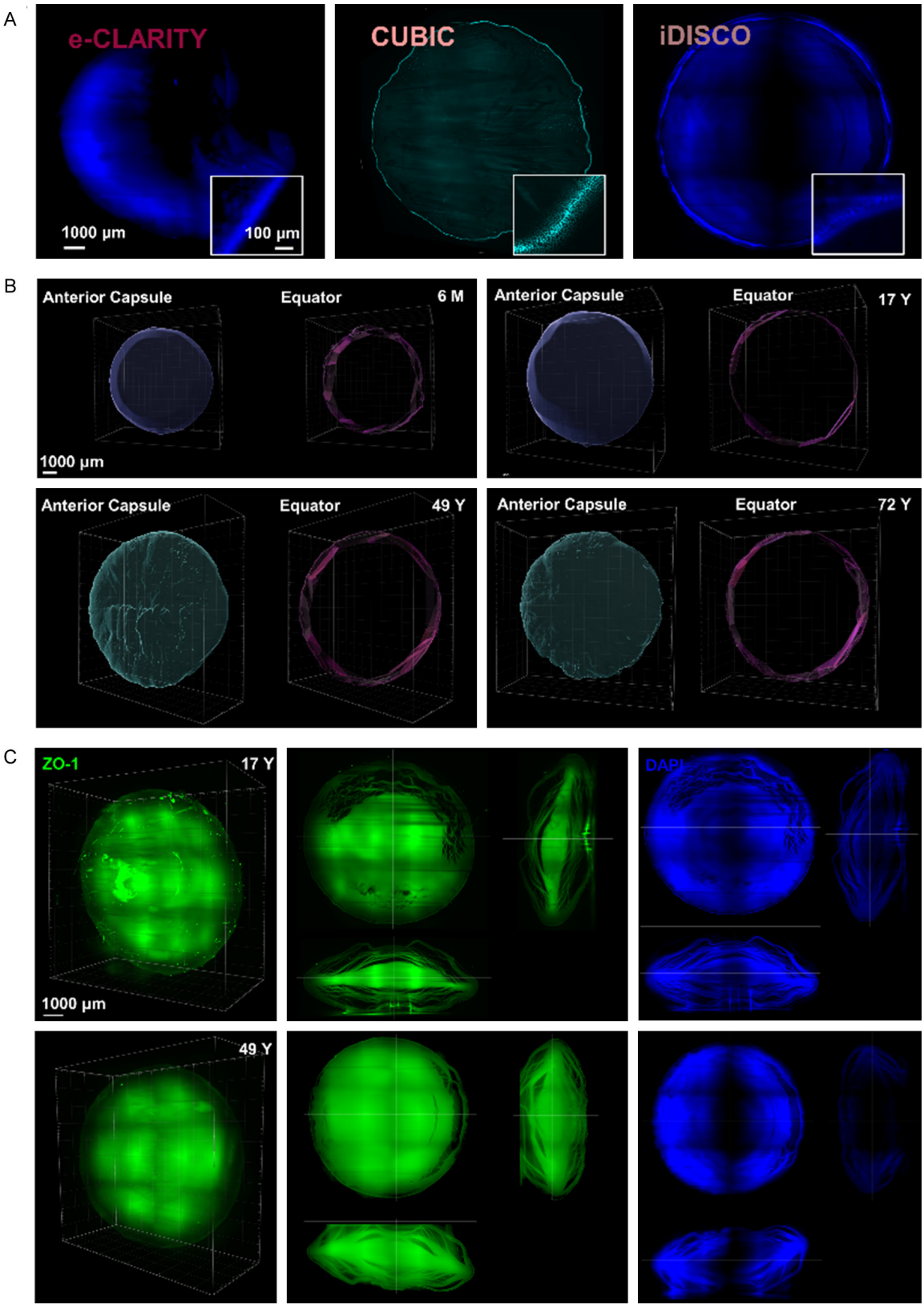

D

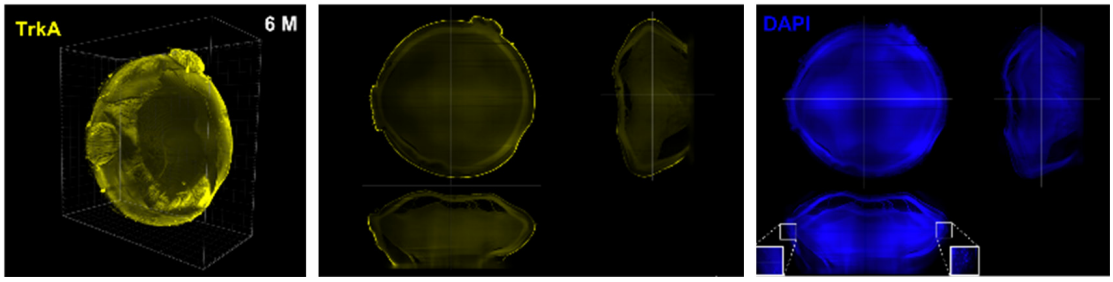

Supplementary Figure 2. Representative 3D views of the molecular and cellular maps of the human lens. A. Randomly chosen planes magnified to show the comparison of nuclear immunostaining efficacy (dark blue for DAPI and light blue for PI) using the different clearing methods. B. Reconstructed surface of the anterior capsule and equator of the 6 M, 17 Y, 49 Y, and 72 Y lenses. C. 3D view of ZO-1 (left) together with three views from the front, side, and top of ZO-1 (middle) and DAPI (right) in addition to the top panel for the 17 Y lens and the bottom panel for the 49 Y lens. D. 3D view of TrkA (left) together with three views from the front, side, and top for TrkA (middle), and DAPI (right) in the 6 M lens.